Monthly Notices
of the
ROYAL ASTRONOMICAL SOCIETY

MNRAS **481,** 4361–4371 (2018)
Advance Access publication 2018 September 26

doi:10.1093/mnras/sty2559

Assessment of Phobos gravity field determination from both near polar and near equatorial orbital flyby data

J. G. Yan,[1,2]★ X. Yang,[1] M. Ye,[1,3]★ T. Andert,[4] W. T. Jin,[1] F. Li,[1] S. G. Jin[5] and J. P. Barriot[1,3]

[1]*State Key Laboratory of Information Engineering in Surveying, Mapping and Remote Sensing, Wuhan University, 129 Luoyu Road, Wuhan 430070, China*
[2]*Space Science Institute, Macau University of Science and Technology, Avenida Wailong, Taipa, Macau 999078, China*
[3]*Observatoire Géodésique de Tahiti, University of French Polynesia, BP 6570, F-98702 Faa'a, Tahiti, French Polynesia*
[4]*Institute of Space Technology and Space Applications, Universität der Bundeswehr München, Neubiberg 85579, Germany*
[5]*Shanghai Astronomical Observatory, Chinese Academy of Science, Shanghai 200030, China*

Accepted 2018 September 15. Received 2018 September 14; in original form 2017 November 1

ABSTRACT

The C_{20} and C_{22} coefficients of the Phobos gravity field are key parameters to constrain the internal structure of the Martian moon, but reliable observed values of these parameters are still missing. In this paper, we demonstrate, through a combination of forward and inverse modelling of simulated Doppler spacecraft tracking data collected from the Earth, that a Phobos flyby along a near polar Mars orbit is optimal when determining the C_{20} coefficient, and further, that a near equatorial flyby Mars orbit is optimal for determination of the C_{22} coefficient. Therefore, the combination of a near polar and a near equatorial orbit is an effective way to determine the Phobos C_{20} and C_{22} gravity field coefficients. This work provides a reference for a future Chinese Mars mission.

Key words: gravitation – methods: data analysis – planets and satellites: fundamental parameters.

1 INTRODUCTION

Phobos is one of the two natural satellites of Mars, and has been a research target since the beginning of Mars exploration. Scientific investigations of Phobos date back to 1970s, with the Mariner 9, Viking 1 and 2, and Phobos-2 missions. Over the last 25 yr, the Mars Global Surveyor, Odyssey, Mars Reconnaissance Orbiter (MRO), and Mars Express (MEX) collected tracking data including optical and radioscience data, to better assess the mass of Phobos (Christensen et al. 1977; Tolson et al. 1977; Williams et al. 1988; Kolyuka et al. 1990; Konopliv et al. 2006, 2011, 2016; Rosenblatt et al. 2008; Andert et al. 2010; Pätzold et al. 2014a,b). The Phobos gravity field will also be the main target of future Mars projects including the MMX (Kuramoto et al. 2017) and DePhine missions (Oberst et al. 2018).

There are two main hypotheses concerning the origins of Phobos, capture, and *in situ* formation scenarios. The capture scenario involves a close third body, or a braking mechanism but fails to explain the equatorial orbit (Burn 1992). The *in situ* formation scenario describes that Phobos formed in a Mars orbit, perhaps from a material disc originating from a collision by an intruding asteroid with a former Mars moon or a former larger Mars moon destroyed by tidal forces exerted by Mars (Burn 1992; Singer 2007), or from the re-accretion of debris blasted into Mars orbit after a large body impacted Mars (Craddock 2011). The in-orbit accretion from a debris disc is currently the favoured hypothesis (Andert et al. 2010; Rosenblatt 2011; Rosenblatt et al. 2016; Pätzold et al. 2014a). A better understanding of Phobos gravity field will provide constraints for the study of its origin.

The geophysical bulk parameters of the internal structure of Phobos, such as mass M, volume V, porosity, bulk density ρ, the dissipation constant Q, and the Love number k2, will help to constrain the hypothesis about its origin (Lambeck 1979; Mignard 1981; Rosenblatt 2011). For example, Pätzold et al. (2014a) derived the currently most precise bulk density of Phobos ($\rho = 1862 +/- 30$ kg m^{-3}), from the ratio of mass (from Doppler data) to volume (from imagery, Willner et al. 2010), and concluded that the moon is highly porous and was probably formed *in situ* by re-accretion of in-orbit debris disc material.

There are two different approaches to solve for the global geophysical parameters GM from orbital dynamics: flybys and long-term interaction on spacecraft orbits (Pätzold et al. 2014b). The highly elliptical near polar orbit of MEX allows several close flybys to Phobos every 5 months (Witasse et al. 2014; Pätzold et al. 2016). Andert et al. (2010) and Pätzold et al. (2014a) processed the 2006, 2008, and 2010 MEX flyby data. The best GM estimate was determined to be $(0.7072 \pm 0.0013) \times 10^{-3}$ km^3 s^{-2} at a closest flyby distance of 77 km (flyby in 2010), but the C_{20} and C_{22} values were obtained with large error bars (Pätzold et al. 2014a,b). The flyby of

★ E-mail: jgyan@whu.edu.cn (JGY); mye@whu.edu.cn (MY)

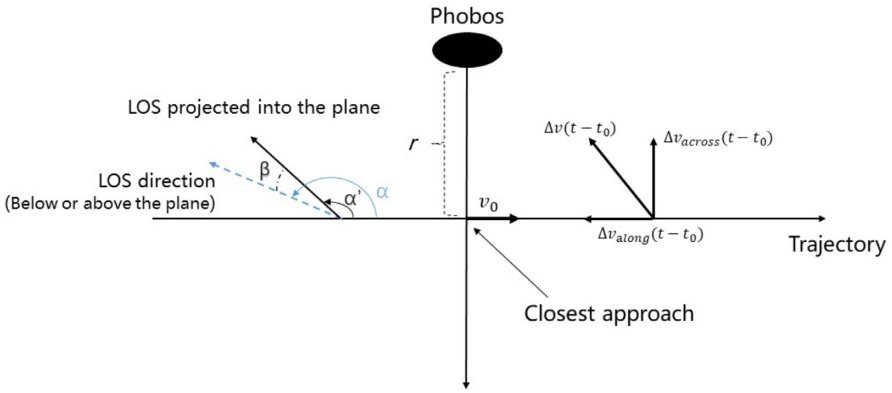

Figure 1. The flyby geometry at Phobos.

2013 with a closest approach distance of 59 km did not provide any improvements in the mass or the gravity field because of the still insufficient precision of the ephemeris of Phobos at the time of the flyby (Pätzold, personal communication).

In consideration of the limited resolution of current polar flyby data, we investigated the potential contribution of a near equatorial flyby of Phobos. The results demonstrate an improvement in the low-degree gravity field solution for Phobos. The paper is organized as follows: theory and methods are presented in Section 2. In Section 3.1, we present a near polar flyby simulation, in Section 3.2 a near equatorial flyby simulation, and in Section 3.3 the combined case. Conclusions are drawn in Section 4.

2 THEORY AND METHODS

Currently the most accurate way to determine the mass of a small celestial body is from radio tracking data collected from a spacecraft during a close flyby (Anderson et al. 1992). The attracting force pulls the spacecraft towards the body, changing its trajectory and its velocity. The magnitude of the final velocity change depends on the closest approach distance and relative velocity, the geometric configuration, and of course the mass and gravitational field of the celestial body. The changing velocity can be observed as an additional Doppler shift on the transmitted radio carrier frequency in the receiver of the ground station antenna by

$$\Delta f = -f_0 \cdot \frac{\Delta v_r}{c}, \tag{1}$$

where Δf is the additional Doppler shift caused by the changed velocity, f_0 is the frequency of the radio carrier (usually X-band at 8.4 GHz), Δv_r is the changed relative velocity along the line-of-sight (LOS) between the spacecraft antenna and the direction to Earth and c is the speed of light. If a coherent two-way radio link is used, then the Doppler shift doubles.

In a two-body system (attracting body and the spacecraft) not considering any forces other than that attracting force acting on the spacecraft, the Doppler shift of the radio carrier frequency f_0 transmitted by the spacecraft in a two-way radio link mode, due to the changed velocity by the attracting force, could be expressed as at closest approach ($t = t_0$) (Pätzold et al. 2001, 2011; Tyler et al. 2009)

$$\Delta f\,(t = t_0) = 2 f_s \frac{GM}{d v_0 c}\left(\cos\,\alpha' - \sin\,\alpha'\right)\cos\,\beta \tag{2}$$

and at post-encounter ($t = \infty$)

$$\Delta f\,(t = \infty) = 4 f_s \frac{GM}{d v_0 c}\sin\,\alpha'\cos\,\beta, \tag{3}$$

where d is the distance between the spacecraft and the body at closest approach, v_0 is the relative velocity at the closest approach position, α' is the angle between the orbit and the LOS projected into the flyby plane, and β represents the angle between the LOS and the flyby plane (Fig. 1). Therefore, a slower relative velocity and a closer distance with respect to the body will increase the final Doppler frequency shift, which also contains the information on GM. These two relations are simplified, but nevertheless, useful for a zero-th order estimate of the expected frequency shift based on the likely geometry of a flyby.

The gravitational acceleration exerted by Phobos on a spacecraft can be ideally expressed as

$$\boldsymbol{g} = \mathbf{M}^{\mathbf{T}}\,\nabla \boldsymbol{U}\,(\mathbf{M}\,(\boldsymbol{r})), \tag{4}$$

where $\boldsymbol{r}$ is the spacecraft position vector with respect to the Phobos gravity centre, $\mathbf{M}$ is the rotation matrix from the inertial reference frame to the Phobos body-fixed frame with $\mathbf{M}^{\mathbf{T}}$ being its inverse, and $\boldsymbol{U}$ is the gravity potential of Phobos expressed w.r.t. this body-fixed frame, while ∇ is the Laplace operator.

In real cases, the components $\mathbf{M}$ and $\boldsymbol{r}$ in equation (4) are contaminated by errors or biases, inducing an error $\delta\boldsymbol{g}$ on $\boldsymbol{g}$:

$$\boldsymbol{g} + \delta\boldsymbol{g} = (\mathbf{M} + \delta\mathbf{M})^T \nabla\left((\boldsymbol{U} + \delta\boldsymbol{U})\left((\mathbf{M} + \delta\mathbf{M})\,(\boldsymbol{r} + \delta\boldsymbol{r} + \Delta\boldsymbol{r})\right)\right), \tag{5}$$

where $\Delta\boldsymbol{r}$ is a possible shift between the centre of gravity and the system of coordinates used for the computation of $\boldsymbol{U}$. In this simulation, we used the priori Phobos gravity field up to degree and order 20 of Shi et al. (2012) computed from the shape model proposed by Willner et al. (2010) under a constant density hypothesis. The shape model was derived from a network of control points at the surface of Phobos that are located with respect to the IAU2009 reference frame (Archinal et al. 2011); therefore the gravity field model is expressed with respect to this frame.

As stated in the Shi et al. (2012) paper, 'since the control points are tied to the centre of Phobos from the ephemerides, the origin of this reference system neither coincides with the centre of figure nor the centre of mass'. This is why we added the $\Delta\boldsymbol{r}$ term in equation (5). This error is small, in the range of 100 m, with respect to the sphere radius of 14 km (Shi et al. 2012), but 10 times larger than the equivalent shift for the Moon, which is already considered very large. This explains the presence of small non-zero C_{10}, C_{11}, and

Table 1. The configuration of the flyby simulations

Item	Detailed description
Martian gravity field	MRO120D (Konopliv et al. 2016)
N-body perturbation	Sun, planets, Phobos, and Deimos
Solar radiation	Simple model
Post-Newtonian effect	Sun and planets
Mars solid tidal perturbation	Love number k2 = 0.169 ± 0.006 (Konopliv et al. 2016)
Atmosphere model	Mars climate data base (Forget et al. 1999)
Initial coordinate	Mars ICRF (Archinal et al. 2011)
Mars body-fixed frame	Pathfinder model with updated orientation parameters (Konopliv et al. 2016)
Phobos body-fixed frame	IAU model (Archinal et al. 2011)
Tracking station coordination correction	Earth solid tides, ocean tides, and polar tide (Mathews et al. 1997)

Table 2. Budget of errors

	Forward modelling	Inverse modelling
Phobos gravity field	20 × 20 gravity field model	2 × 2 gravity field model
Phobos rotation model	IAU model	0.01°errors in α, δ, and W
Phobos ephemeris	No errors	10–500 m errors in Tangent direction of Phobos orbit
Noise level of observables	± 0.055 mm s^{-1} (70-m) ± 0.065 mm s^{-1} (66-m)	

S_{11} coefficients in their gravity model. This also implies that all the other harmonic coefficients are affected, also to a small level, by this shift between the IAU2009 reference and the gravity centre frames. Moreover, the orientation of the IAU2009 reference frame does not coincide with the principal axis of Phobos. Shi et al. (2012) estimated that this misalignment to be in a magnitude of 1.2 deg. This explains the presence of small C_{21}, S_{21}, and S_{22} coefficients in their model, corresponds to the $\delta\mathbf{M}$ term in equation (5).

However, this is not the end of the story. The orbit of Phobos is also ill-constrained (Jacobson & Lainey 2014; Lainey et al. 2016); and at the moment, the orbital accuracy of Phobos is only in the range of 100–1000 m, as estimated from Viking 1–2, Phobos 2, Mariner 9, and MEX spacecraft optical observations. The accuracy of this estimate was degraded by a few kilometres, as the orbital data were not constrained by observations. This corresponds to the $\delta\boldsymbol{r}$ term in equation (5). Equation (5) shows that the $\delta\boldsymbol{r}$ and the $\Delta\boldsymbol{r}$ cannot be separated. These values are of the same order of magnitude when the orbit of Phobos is well constrained, otherwise $\delta\boldsymbol{r}$ can be 10 times larger than $\Delta\boldsymbol{r}$. Equation (5) is also telling us that the modelling of the physically meaningful C_{20} and C_{22} components is not directly possible without a good knowledge of the location of the gravity centre of Phobos and of the orientation of its principal axis.

The $\delta\boldsymbol{U}$ error is more subtle than errors discussed previously in this section. This error, termed a bias by omission, from a mathematical point of view, occurs because the gravity field is not limited to degree and order two, but extends to infinity. For our simulation, as already stated, we used the gravity field model, up to degree and order 20, from Shi et al. (2012) for forward modelling. For the inverse modelling, we limited the harmonic expansion of $\boldsymbol{U}$ up to degree and order 2, leading to the $\delta\boldsymbol{U}$ term in equation (5). Again, this $\delta\boldsymbol{U}$ term is small, and probably buried in the Doppler measurement noise, but equation (5) shows that the small errors $\Delta\boldsymbol{r}$, $\delta\mathbf{M}$, and $\delta\boldsymbol{U}$, without forgetting $\delta\boldsymbol{r}$, can be large, are highly interconnected in a non-linear way, thus, we have to be careful not to ignore too many small terms just because they are small. In this study, we therefore chose to solve (inverse modelling) for the *GM*, and the full sets coefficients of first and second degrees of the gravity field of Phobos from simulated Doppler data computed from the gravity model up to degree and order 20 in Shi et al. (2012). This gravity field model was given in the IAU2009 frame, i.e. including an a priori $\Delta\boldsymbol{r}$ term (forward modelling). For inverse modelling, we added a $\delta\boldsymbol{r}$ bias on the coordinates of Phobos from the ephemeris, and a $\delta\mathbf{M}$ bias on the rotation $\mathbf{M}$ following equation (5). We cannot, of course, solve the rotation matrix $\mathbf{M}$ from a flyby of a few minutes. We also cannot solve separately the $\Delta\boldsymbol{r}$ and the $\delta\boldsymbol{r}$ terms, so their sum was determined through the C_{10}, C_{11}, and S_{11} coefficients, representing the shifts in the position of the gravity centre of Phobos, as scaled by the main radius of Phobos used in the gravity field model. There is also another reason to solve the C_{10}, C_{11}, and S_{11} coefficients, i.e. not to force them to zero. If we do that, the inverse least-square process will simply compensate by biasing the determination of the second-order coefficients.

It is also clear, that in the real case, the gravity coefficients of Phobos cannot deviate by a large amount of the coefficients computed from the shape model under a constant density hypothesis. Thus, we can use these values as a priori parameters during inverse modelling employing realistic but large bounds.

Finally, realistic noise (i.e. not purely Gaussian, see Asmar et al. 2005) was added to our simulated Doppler data, created from data processing residuals of actual MEX Doppler data. All other error sources and simulation assumptions not related to Phobos itself, are presented in the next sections. Tables 1 and 2 summarize our assumptions and the error budget.

3 FLYBY SIMULATIONS AT PHOBOS AND GRAVITY FIELD SOLUTIONS

The complete force models on the spacecraft include the latest JPL Martian gravity field model MRO120D (Konopliv et al. 2016), the post-Newtonian effect (Moyer 2005; Huang et al. 1990), the third-body perturbation from Mars and the Martian moons, the solar radiation pressure as well as the atmospheric drag at the low orbit altitudes. The atmospheric parameters employed in the atmospheric

Table 3. Phobos low-degree gravity field coefficients used as the 'true' model to generate the synthetic Doppler data. These values are from Shi et al. (2012). The synthetic data were computed by considering their gravity field model up to degree and order 20. The reference radius of Phobos is 14 km.

Parameter	A priori value (10^{-2})	A priori error bar (10^{-2})		
		100 per cent	50 per cent	30 per cent
C_{10}	−0.350	±0.350	±0.175	±0.105
C_{11}	0.304	±0.304	±0.152	±0.091
S_{11}	−0.246	±0.246	±0.123	±0.074
C_{20}	−2.957	±2.957	±1.979	±0.887
C_{21}	0.085	±0.085	±0.042	±0.025
C_{22}	1.536	±1.536	±0.768	±0.461
S_{21}	−0.037	±0.037	±0.019	±0.011
S_{22}	0.039	±0.039	±0.020	±0.012
GM (10^5 m^3s^{-2})	7.0721	±0.070	–	–

drag force are a function of altitude, and they are taken from the Mars Climate Data base (MCD) (Forget et al. 1999; González-Galindo et al. 2009; Millour et al. 2015). The DE421 ephemeris (Folkner et al. 2008) and the new Phobos ephemeris of Lainey et al. (2016) were also employed in the simulations based on our in-house Mars Gravity Recovery and Analysis Software (Yan et al. 2017a,b). In Table 1, we provide a list of the settings used.

Table 2 shows the budget of errors in our simulations. During the MEX/Phobos flyby 2013 observed by the 70-m antenna of the NASA Deep Space Network (DSN) in Madrid, the frequency noise of the Mars Express Radio Science experiment (MaRS) was ±0.055 mm s^{-1} or ±2 mHz at X-band with a 1σ standard deviation at 1 s integration time. This noise was added to the simulated MEX flyby Doppler observables to obtain realistic observables. Considering the similar antenna diameter of the Jiamusi station (66-m), a 1σ standard deviation of ±0.065 mms^{-1} or ±2.4 mHz at X-band at 1 s integration time was added to the simulated near equatorial orbit flyby Doppler observables. The prime ground station antennas were DSS-63 70-m antenna in Madrid, Spain (for the simulated MEX flyby) and the 66-m Chinese station in Jiamusi (for the future mission in a near equatorial orbit flyby) in the simulation.

The error magnitude on the right ascension α, declination δ, and W is about ±0.01° (Archinal et al. 2011). During the inverse modelling, we successively applied a 0.01°and a −0.01°error to these three angles, and we found that the induced maximum difference w.r.t the true value of the gravity field coefficients was only around 0.07 per cent. Therefore, we only present simulation results for an 0.01°error in the α, δ, and W angles. In addition, we introduced an error on the ephemeris of Phobos by adding some δt shift in time to ephemeris time, resulting in a position shift ranging from 10 to 500 m, mainly along the tangent direction of the orbit of Phobos.

As already stated in the previous section, we solved the inverse problem through a least-square process. The unknowns were the Phobos gravity field coefficients up to degree and order two, including degree zero (the *GM*) and degree one. We used a priori values as the forward values, as the reconstructed values must not differ significantly from these values from a physical point of view. In a real flyby, this means that the modelled values cannot be too far from the values computed from the shape model under a constant density hypothesis. We also stress that to use zero as a priori values for the first- and second-degree coefficients in the inverse modelling is implicitly not reasonable, as Phobos moon is not a perfect homogeneous sphere. We therefore chose to solve the gravity coefficients with a priori error bars up to 100 per cent (corresponding to an a priori 1σ deviation) and solved the well-constrained Phobos *GM* with a priori error bar of 1 per cent. We tested three levels (Table 3) of a priori error bars of the gravity coefficients in the simulation (100, 50, and 30 per cent of the value employed in the forward modelling).

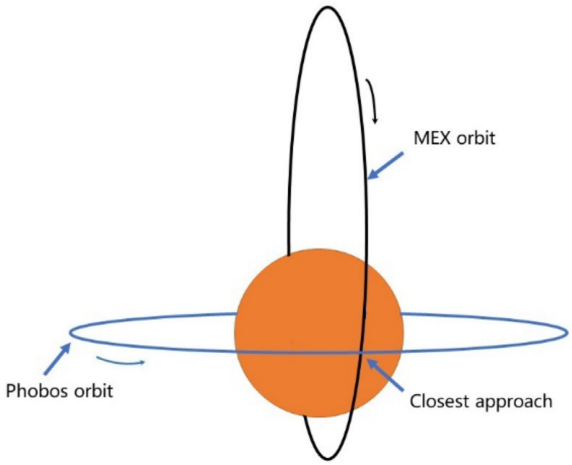

Figure 2. The near polar orbit flyby geometry.

3.1 Simulated MEX flyby (near polar spacecraft orbit)

MEX made its closest approach to Phobos on 2013 December 29 at a distance of 59 km. Fig. 2 illustrates the flyby scenario. During the flyby, the angle between LOS and the MEX orbit plane closed to 6 deg, which means a high orbit quality (edge on orbit) for precise orbit determination.

Fig. 3 shows the perturbation magnitude of several low degree and order coefficients for the Phobos gravity field. When the spacecraft arrived at the closest distance to Phobos in the simulation, the accelerations caused by C_{10}, C_{11}, S_{11}, C_{20}, and C_{22} were dominant and their values reached 10^{-6} m s^{-2} level. The accelerations caused by C_{21}, S_{21}, and S_{22} were at the 10^{-7}∼10^{-8} m s^{-2} level near the closest approach.

Fig. 4 presents the change in relative velocity in the LOS direction, due to the attraction of Phobos gravity field. The differential velocity (synthetic data minus predicted observables not considered Phobos gravity field) increases abruptly within a minute when the MEX spacecraft approached Phobos, with an inversed S-shaped signature after the closest approach. The feature is caused by the large velocity perturbation during the pericentre pass after closest approach

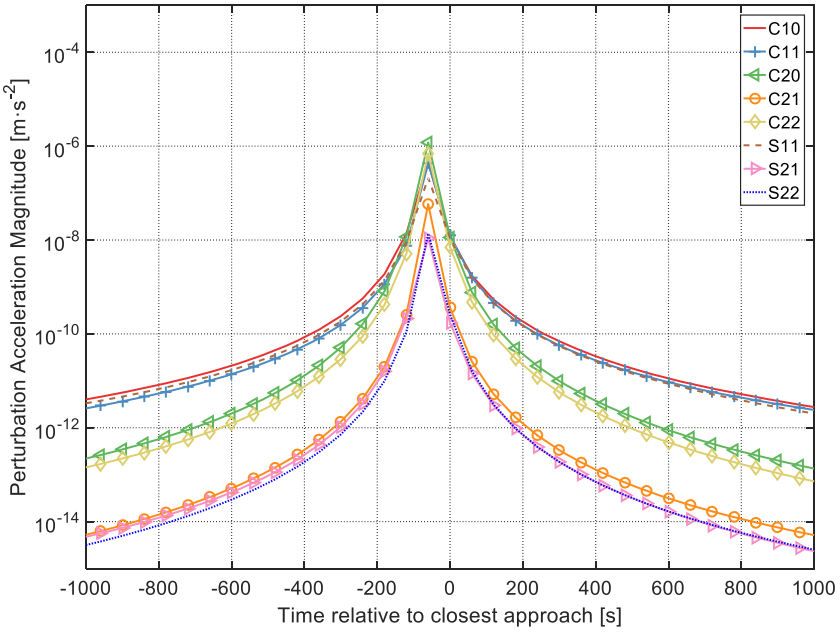

Figure 3. The magnitude of the perturbation accelerations of several simulated Phobos gravity field coefficients for the near polar flyby scenario.

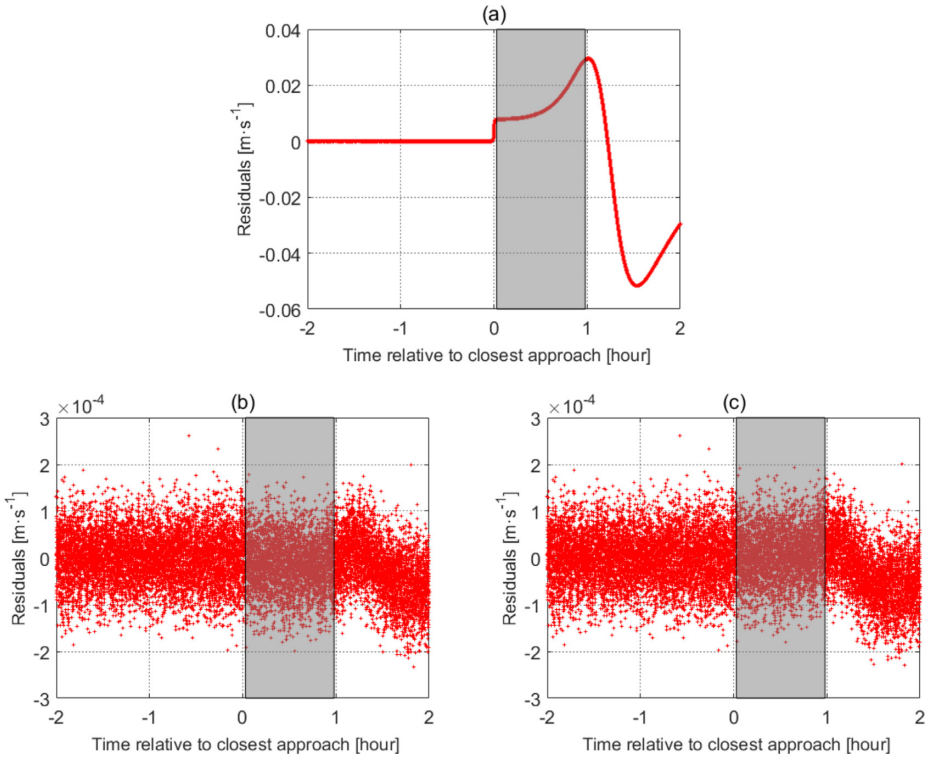

Figure 4. Frequency residuals at X-band (simulated perturbed Doppler frequency minus the simulated unperturbed Doppler frequency) for a time ±2 h about closest approach to Phobos. The grey area marks about 1 h radio signal loss due to a Mars occultation. Panel (a): the frequency residuals (GM, C_{20}, and C_{22}); panel (b): contribution to the frequency residuals in Panel (a) from C_{20}; panel (c) contribution to the frequency residuals from C_{22}.

We ignored the tracking gap in our solution. The close flyby of MEX 2013 occurred during a Mars occultation season when the spacecraft disappeared behind the planetary disc in every orbit as seen from Earth (Pätzold et al. 2016). There was a tracking gap of 1 h starting 4 min after the closest approach. In our simulation however, we did not consider this tracking gap because it was a simulation of a near polar orbit flyby case, and therefore not relevant. The grey area in Fig. 4 marks out the occultation duration.

Table 4. The orbital elements applied in the simulation

Semimajor axis (km)	Eccentricity	Inclination (deg)	Right ascension of ascending node (deg)	Argument of perigee (deg)	Mean anomaly (deg)
7602.52	0.495	22.011	220.256	322.689	128.407

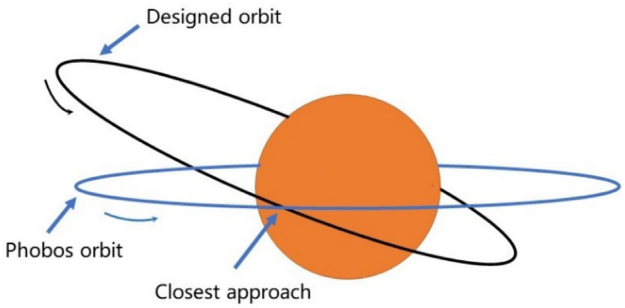

Figure 5. The near equatorial flyby geometry.

3.2 Simulated flyby for a near equatorial orbit

The orbital elements of the near equatorial orbit in the Mars inertial frame are presented in Table 4. The tracking station for this near equatorial orbit flyby simulation was the 66-m size antenna at Jiamusi. The other settings were the same as those in Table 1. The flyby geometry is shown in Fig. 5.

The orbit plane forms with the LOS direction a small angle of 3 deg therefore we have an almost in-plane flyby. Fig. 6 illustrates the magnitudes of the perturbation acceleration computed from the Phobos gravity field.

Similar to the MEX flyby 2013, a closest approach of about 59 km was selected for the simulation of the near equatorial flyby. As mentioned in Section 3.1, the accelerations caused by C_{20}, C_{22}, C_{10}, C_{11}, and S_{11} were dominant in our results. The perturbations from C_{21}, S_{21}, and S_{22} were much lower in the order of 10^{-8} m s^{-2}.

About 1.5 h after the closest approach in the simulation, the Doppler residual reach a maximum, as the spacecraft passes through the pericentre at about 1.5 h after the flyby (Fig. 7). As already mentioned in Section 3.1, a large velocity perturbation occurred during the pericentre pass where the spacecraft velocity is biggest and therefore the residuals are higher too.

3.3 Solutions for the two flybys and discussion

Fig. 8 summarizes our inverse modelling results of degree 2, for different choices of the a priori constraints and Phobos ephemeris errors. Detailed results are provided in the supplementary material. From Fig. 8 we can clearly see that a near polar orbit flyby is better in resolving the C_{20} coefficient while a near equatorial orbit flyby is better in resolving the C_{22} coefficient. The reason is that the zonal harmonic corresponding to C_{20} has an equatorial symmetry only, while the sectorial harmonic corresponding to C_{22} has an orange-like symmetry. As the Phobos axis of rotation is almost aligned with the Mars rotation axis, and because the flyby is nearly instantaneous, a near polar orbit only senses the C_{20} coefficient, as the C_{22} coefficient has almost the same effect on the spacecraft orbit during the flyby. Inversely, during an equatorial flyby, the C_{20} coefficient has almost the same effect on the spacecraft orbit, and the orange-like nature of the sectorial C_{22} coefficient is inducing a full signature on the spacecraft orbit. By combining the two flyby geometries, it is then natural to be able to solve for the two coefficients.

For the other second-order gravity field coefficients, e.g. C_{21}, S_{21}, and S_{22}, the a posteriori error bars are close to the a priori error bars, with almost no improvement even with a decrease in the Phobos ephemeris error. This is coherent with the IAU 2009 body fixed frame that is close to the main principal axis frame of Phobos. We can also clearly see on Fig. 8 that we need an accuracy of 100–200 m maximum on the ephemeris of Phobos to obtain a reliable modelling of the C_{20} and C_{22} coefficients.

The degree one coefficients of a gravity field model could be expressed as (Hofmann & Moritz 2006):

$$C_{10} = \frac{z}{R_0} \tag{6}$$

$$C_{11} = \frac{x}{R_0} \tag{7}$$

$$S_{11} = \frac{y}{R_0}, \tag{8}$$

where $(x,\ y,\ z)$ are the coordinates of centre-of-mass (COM) in a body-fixed frame, and R_0 represents the reference radius of Phobos. As mentioned in Section 2, we cannot solve separately the $\Delta \boldsymbol{r}$ and the $\delta \boldsymbol{r}$ terms for equation (5), but their sum is determined through the C_{10}, C_{11}, and S_{11} coefficients. Therefore, we use the following expression to describe the accuracy of degree 1 solution:

$$\varepsilon = |\boldsymbol{X}_s - \boldsymbol{X}_0| - \delta \boldsymbol{r}, \tag{9}$$

where the $\boldsymbol{X}_s$ represents the solution of COM coordinates (i.e. x, y, z in equations 6–8), the $\boldsymbol{X}_0$ is the a priori COM coordinates, the $\delta \boldsymbol{r}$ is the ephemeris error we added ranging from 10 to 500 m. The result can be seen in Fig. 9.

Figs 8 and 9 suggest that the combined solution is more sensitive to the ephemeris error in the Phobos orbit rather than each of the individual solutions. Thus, the inverse modelling combining a near equatorial flyby with a near polar flyby has the potential capability to solve the sum of the $\Delta \boldsymbol{r}$ and the $\delta \boldsymbol{r}$ terms.

The power spectrum of a gravity field model (or of its associated error) is invariant by rotation. The formulas to define them are (Hofmann & Moritz 2006, Yan et al. 2012; Yan et al. 2017b):

$$\sigma_n = \sqrt{\frac{\sum_{m=0}^{n} \left(\bar{C}_{nm}^2 + \bar{S}_{nm}^2\right)}{2n+1}} \tag{10}$$

$$\delta_n = \sqrt{\frac{\sum_{m=0}^{n} \left(\bar{\sigma}_{\bar{C}_{nm}}^2 + \bar{\sigma}_{\bar{S}_{nm}}^2\right)}{2n+1}}, \tag{11}$$

where $\bar{\sigma}_{\bar{C}_{nm}}^2$ and $\bar{\sigma}_{\bar{S}_{nm}}^2$ are the error variances of the gravity field coefficients. For completeness, and as we are solving for the whole set of coefficients, we provide these spectrums for the second order in Fig. 10. Fig. 10 shows clearly that the combined solution (polar + equatorial flybys) is superior by one order of magnitude w.r.t. the individual solutions.

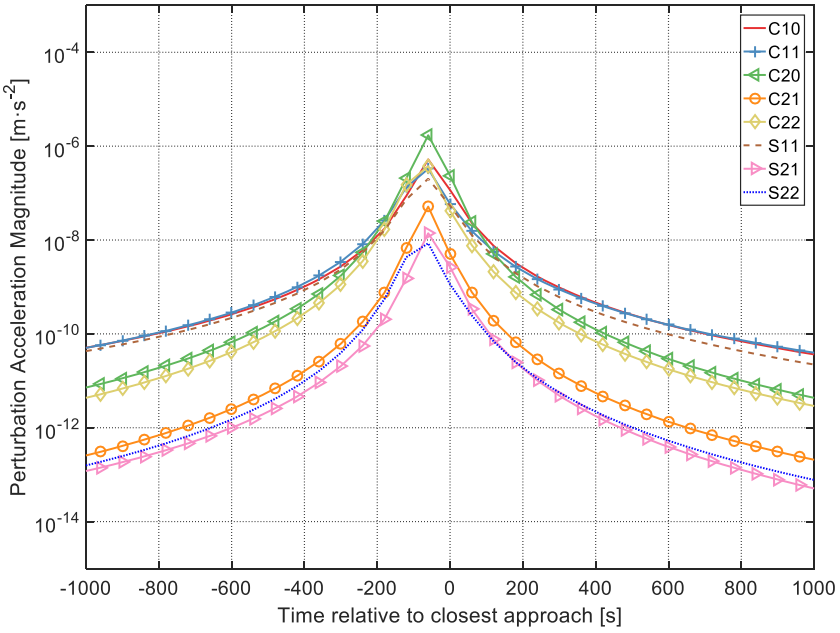

Figure 6. The perturbation accelerations from the simulated Phobos gravity field for the near equatorial flyby case.

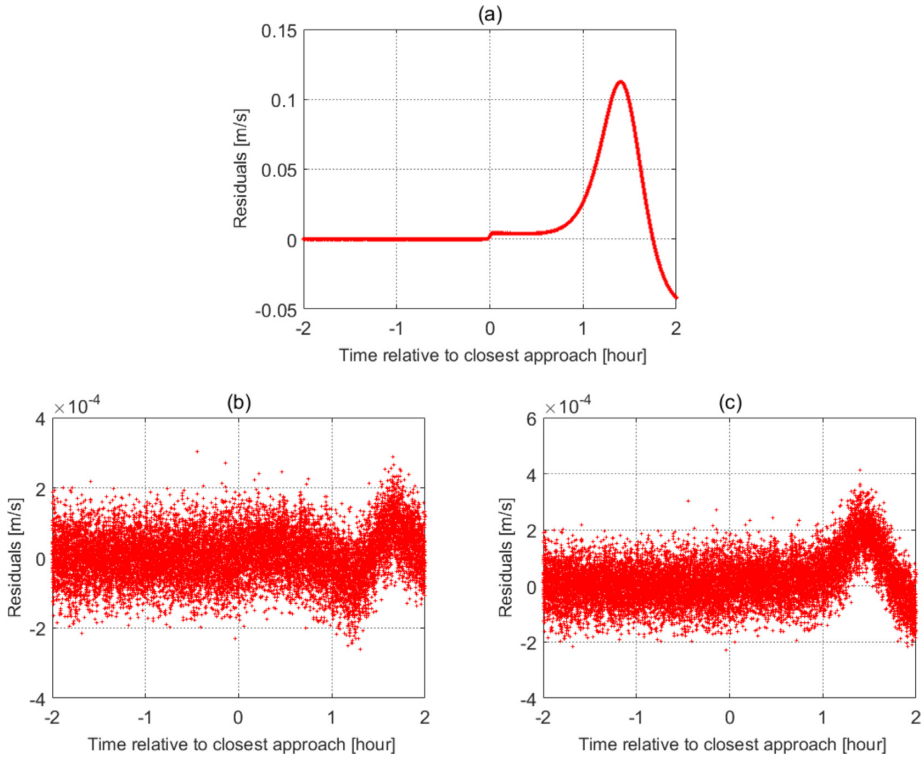

Figure 7. The Doppler velocity residuals from the Doppler velocities from the flyby trajectory perturbed by the simulated Phobos gravity field minus the predicted unperturbed Doppler velocities. Panel (a) is the total Doppler velocity residuals from contributions by GM, C_{20}, and C_{22}; panel (b) is the Doppler residual from C_{20}; panel (c) is the Doppler residual from C_{22}.

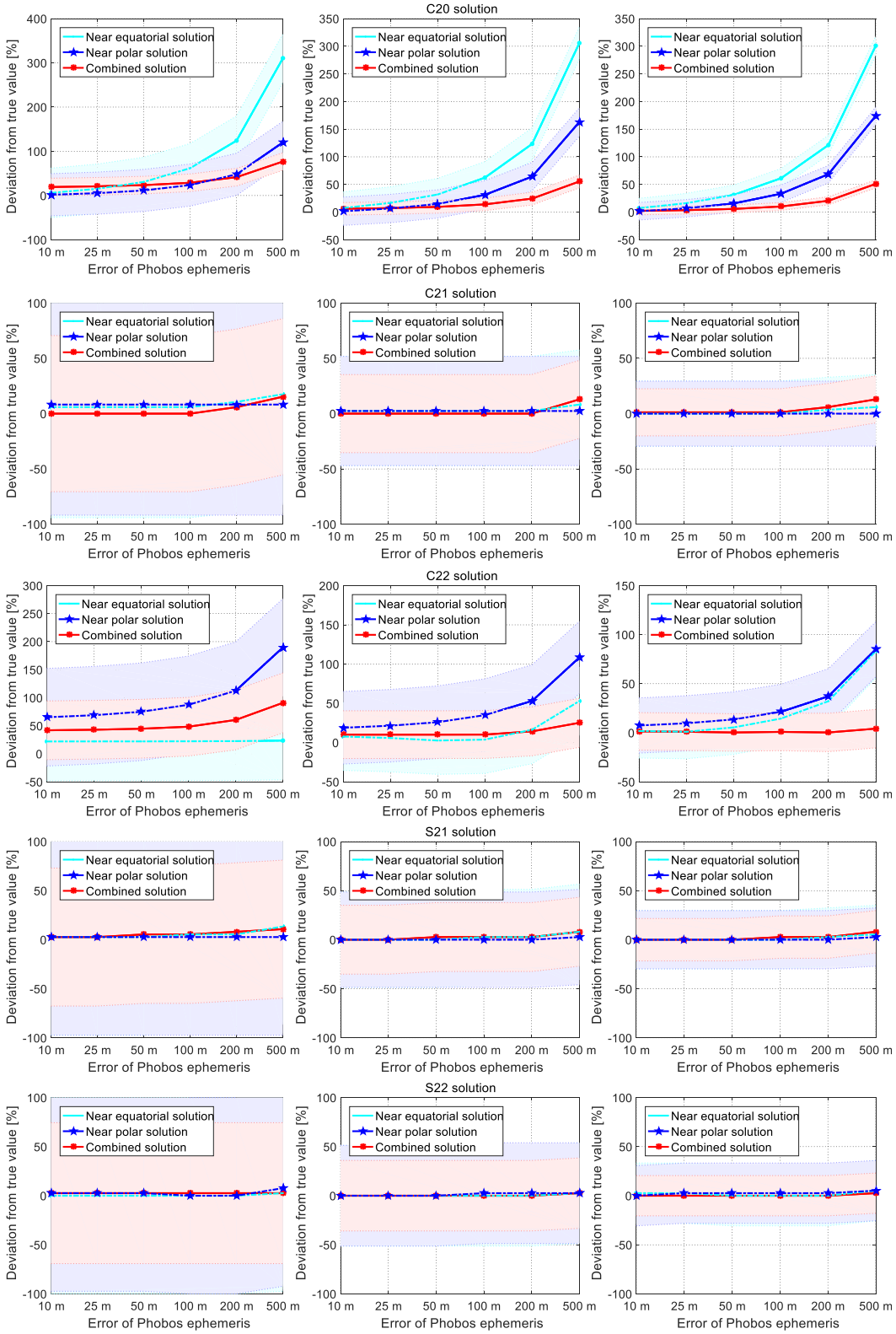

Figure 8. Simulation of the modelling of the second degree and order gravity coefficients of Phobos, for the two orbit flybys (separated and combined). The left-column corresponds to the solution of the gravity field with an a priori error bar of 100 per cent; the mid-column corresponds to the solution of the gravity field with an a priori error bar of 50 per cent; the right column corresponds to a gravity field solution with an a priori error bar of 30 per cent. The GM a priori error bar is set to 1 per cent. The horizontal axis on each sub-figure corresponds to the a priori Phobos ephemeris. The vertical axis of each sub-figure represents the per centage of the modelled gravity coefficient w.r.t. its true value. The highlighted areas represent the a posteriori error bars.

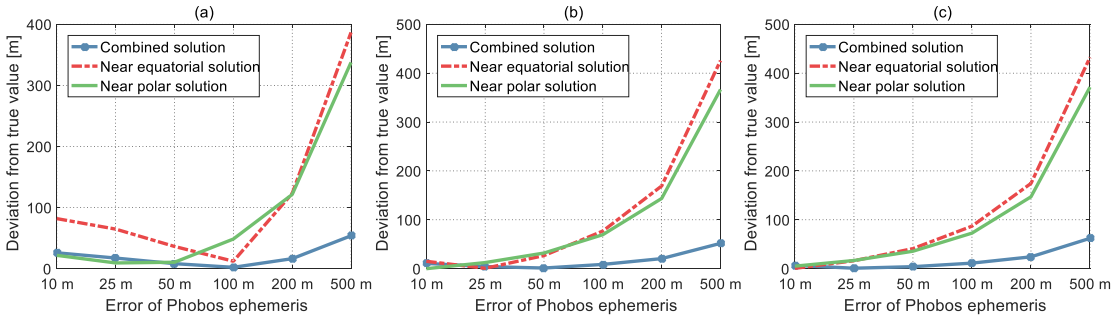

Figure 9. Assessment accuracy of degree 1 coefficients in the inverse modelling with simulated data. Panel (a) corresponds to the solution with an a priori error bar of 100 per cent; panel (b) corresponds to the solution with an a priori error bar of 50 per cent; panel (c) is solution with a priori error bar of 30 per cent. The horizontal axis on each sub-figure is the error on the Phobos ephemeris. The vertical axis represents the ε in equation (9).

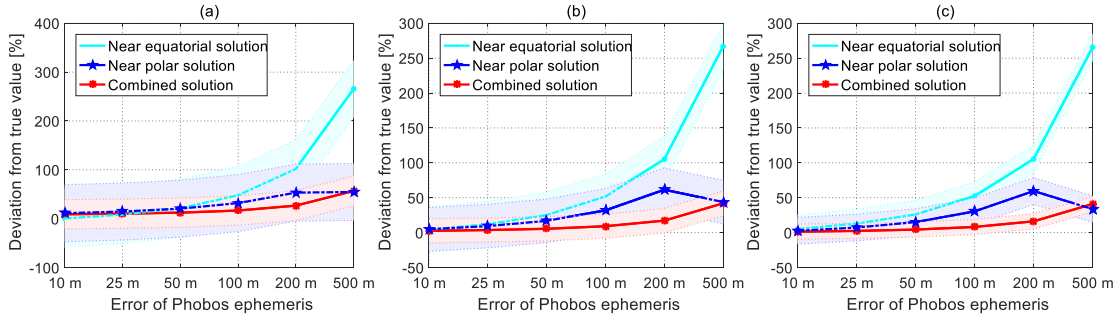

Figure 10. Differences in the degree 2 power spectra between the solution and the 'true' model. Notations are the same as in Fig. 8. The vertical axis of each sub-figure now represents the per centage of the solved σ_n deviation from the σ_n of the 'true' model.

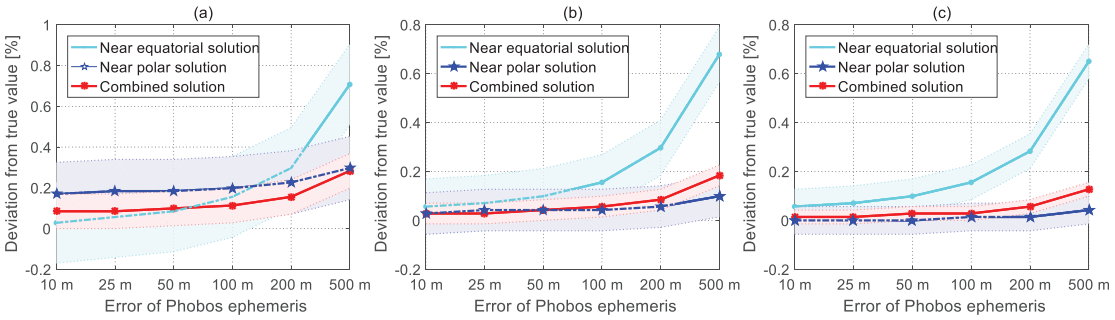

Figure 11. Simulation of the modelling of the Phobos GM coefficient, for the two orbit flybys (separate and combined). Notations are the same as in Fig. 10. A priori error bar of GM coefficient is set to 1 per cent. Panels (a), (b), and (c) correspond to the estimation of the gravity field coefficients with an a priori error bars of 100, 50, and 30 per cent.

We also provide the *GM* coefficient modelling results in Fig. 11. For the already well-constrained Phobos *GM* value, we considered a priori error bar of 1 per cent. Our main result shows that by combining the two flyby geometries, the *GM* a posteriori error bar decreases by almost 50 per cent w.r.t. separate flybys.

For the sake of completeness, we also present the post-fit residuals for the two orbit flybys cases in Fig. 12. The QQ-plots (Wilk & Gnanadesikan 1968) indicate, as they almost follow a linear trend, that albeit we introduced biases in the inverse modelling (i.e. non-Gaussian noise, the major errors stemming from the Phobos ephemeris), our choice of unknowns (the whole set of gravity coefficients) is able to absorb these biases, with residuals that are almost Gaussian.

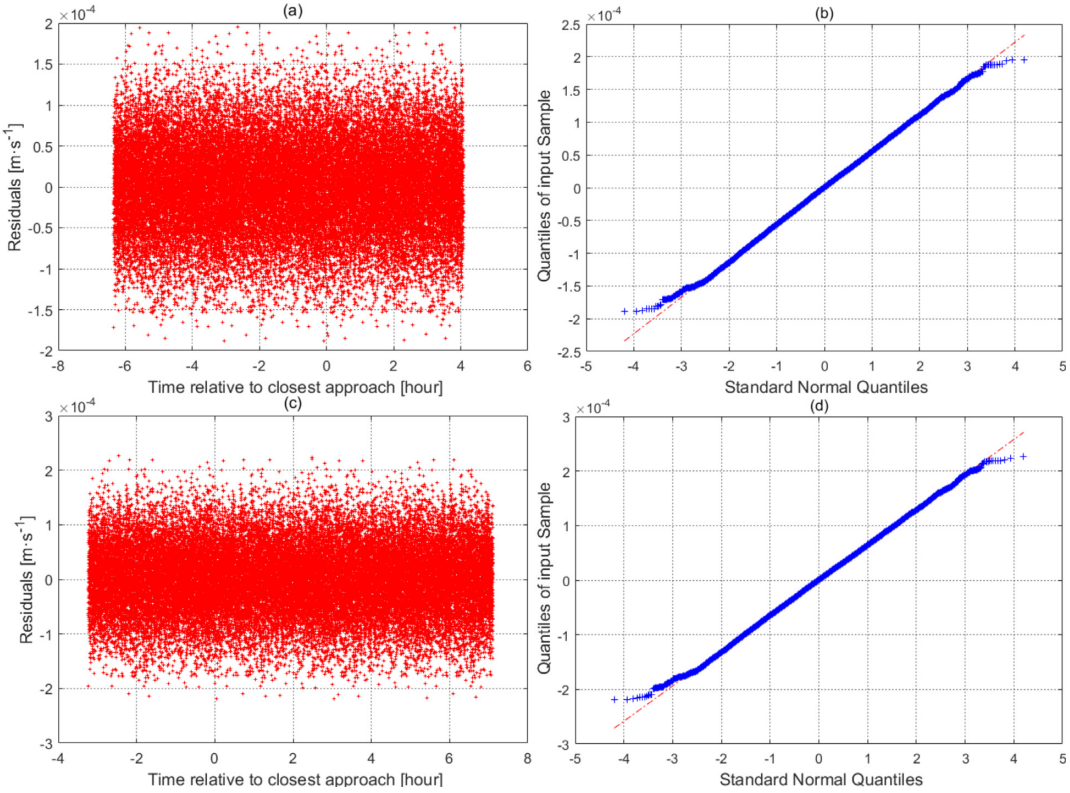

Figure 12. The post-fit residuals for the two orbit flybys case. For briefly, we only plot the case of a priori error bars of 100 per cent and Phobos ephemeris error of 200 m. Panels (a) and (c) are, respectively, the near polar and near equatorial orbit cases. Panels (b) and (d) are relative to the QQ-normal probability plots for those residuals.

4 CONCLUSION

In this paper, we analysed, through a simulation process, the contribution of a near equatorial and a near polar Mars orbit flybys to the modelling of Phobos low-degree gravity field. Our simulation shows that a near polar Mars orbit flyby has better accuracy for the determination of the C_{20} coefficient while a near equatorial Mars orbit flyby has superiority for the determination of C_{22} coefficient. A combined solution provides reliable C_{20} and C_{22} coefficients, provided that the error contaminating the Phobos ephemeris is not too large, with a threshold at about 200 m.

This paper paves the way for a future near equatorial Mars orbit mission that was shown to be a unique complement to Mars mapping missions that are almost all with near polar orbits.

ACKNOWLEDGEMENTS

We are grateful to NASA and ESA for providing models and data to make this research possible. This work is supported by National Scientific Foundation of China (U1831132, 41874010, 41804025), Innovation Group of Natural Fund of Hubei Province (2015CFA011 and 2018CFA087), and China Postdoctoral Science Foundation (2016M602360). The Open Funding of Macau University of Science and Technology (FDCT 119/2017/A3), Open Funding of Guizhou Provincial Key Laboratory of Radio Astronomy and Data Processing (KF201813), and the Opening Project of Shanghai Key Laboratory of Space Navigation and Positioning Techniques (KFKT_201703) also support this work. TA is funded by the German Space Agency (DLR) under the grant 50QM1704. JPB is funded by a DAR grant in planetology from the French Space Agency (CNES).

REFERENCES

Anderson J. D., Armstrong J. W., Campbell J. K., Estabrook F. B., Krisher T. P., Lau E. L., 1992, Space Sci Rev, 60, 591
Andert T. P., Rosenblatt P., Pätzold M., Häusler B., Dehant V., Tyler G. L., Marty J. C., 2010, Geophys. Res. Lett., 37, 9
Archinal B. A. et al., 2011, Celest. Mech. Dyn. Astron., 109, 101
Asmar S. W., Armstrong J. W., Iess L., Tortora P., 2005, Radio Sci., 40, 2
Burns J. A., 1992, in Kieffer H. H., Jakosky B. M., Snyder C., Matthews M. S., eds, Mars. Univ. Arizona Press, Tucson, p. 1283
Christensen E. J., Born G. H., Hildebrand C. E., Williams B. G., 1977, Geophys. Res. Lett., 4, 555
Craddock R. A., 2011, Icarus, 211, 1150
Folkner W. M., Williams J. G., Boggs D. H., 2008, JPL IOM 343R-08-003
Forget F. et al., 1999, J. Geophys. Res., 104, 24155
González-Galindo F., Forget F., López-Valverde M. A., Coll Angelats I., Millour E., 2009, J. Geophys. Res., 114, E04001
Hofmann-Wellenhof B., Moritz H., 2006, Physical Geodesy, Springer, Berlin
Huang C., Ries J. C., Tapley B. D., Watkins M. M., 1990, Celest. Mech. Dyn. Astron., 48, 167
Jacobson R.A., Lainey V., 2014, Planet. Space Sci., 102, 35
Kolyuka Y. F., Ephimov A. E., Kudryavtsev S. M., Margorin O. K., Tarasov V. P., Tikhonov V. F., 1990, Pisma v Astronomicheskii Zhurnal, 16, 396
Konopliv A. S., Yoder C. F., Standish E. M., Yuan D. N., William L. S., 2006, Icarus, 182, 23

Konopliv A. S., Asmar S. W., Folkner W. M., Ö. Karatekin, Nunes D. C., Smrekar S. E., Yoder C. F., Zuber M. T., 2011, Icarus, 211, 401
Konopliv A. S., Park R. S., Folkner W. M., 2016, Icarus, 274, 253
Kuramoto K., Kawakatsu Y., Fujimoto M., Team M.S., 2017, Abstract at: Lunar and Planetary Science Conference. Texas, p. 2086
Lainey V., Pasewaldt A., Robert V., Rosenblatt P., Andert T., Pätzold M., Thuillot W., 2016, A&A, in press
Lambeck K., 1979, J. Geophys. Res., 84, 5651
Mathews P. M., Dehant V., Gipson J. M., 1997, J. Geophys. Res., 102, 20469
Mignard F., 1981, MNRAS, 194, 365
Millour E. et al., 2015, The mars climate database (mcd version 5.2), 10, 1184
Moyer T. D., 2005, Formulation for Observed and Computed Values of Deep Space Network Data Types for Navigation. Vol. 3., John Wiley & Sons, Hoboken
Oberst J. et al., 2018, Adv. Space Res., 62, 2220
Pätzold M., Wennmacher A., Häusler B., Eidel W., Morley T., Thomas N., Anderson J. D., 2001, A&A, 370, 1122
Pätzold M. et al., 2011, Science, 334, 491
Pätzold M., Andert T. P., Tyler G. L., Asmar S. W., Häusler B., Tellmann S., 2014a, Icarus, 229, 92
Pätzold M., Andert T., Jacobson R., Rosenblatt P., Dehant V., 2014b, Planet. Space Sci., 102, 86
Pätzold M. et al., 2016, Planet. Space Sci., 127, 44
Rosenblatt P., Lainey V., Le Maistre S., Marty J. C., Dehant V., P ätzold M., Vanhoolst T., Häusler B., 2008, Planet. Space Sci., 56, 1043
Rosenblatt P., 2011, Astron. Astrophys. Rev., 19, 1
Rosenblatt P., Charnoz S., Dunseath K. M., Terao-Dunseath M., Trinh A., Hyodo R., Genda H., Toupin S., 2016, Nat. Geosci, 9, 581
Shi X, Willner K., Oberst J., Ping J., Ye S., 2012, Sci. China Phys. Mech. Astron., 55, 358
Singer S. F., 2007, Proceedings of the conference held at Moffett Field, California, November 5–8, 2007, First International Conference on the Exploration of Phobos and Deimos, LPI Contributions 1377, 36
Tolson R. H., Blackshear W. T., Mason M. L., Kelly G. M., 1977, Geophys. Res. Lett., 4, 551
Tyler G. L., Linscott I. R., Bird M. K., Hinson D. P., Strobel D. F., Pätzold M., Summers M. E., Sivaramakrishnan K., 2009, New Horizons, The New Horizons Radio Science Experiment (REX). Springer, New York, p. 217
Wilk M. B., Gnanadesikan R., 1968, Biometrika, 55, 1
Williams B. G., Duxbury T. C., Hildebrand C. E., 1988, JPL California Institute of Technology, Pasadena, CA, 91109
Willner K., Oberst J., Hussmann H., Giese B., Hoffmann H., Matz K. D., Roatsch T., Duxbury T., 2010, Earth Planet. Sci. Lett. 294, 541
Witasse O. et al., 2014, Planet. Space Sci., 102, 18
Yan J. G. et al., 2012, Planet. Space Sci., 62, 2012
Yan J. G., Yang X., Ye M., Li F., Jin W. T., Barriot J. P., 2017a, Astrophys. Space Sci., 362, 123
Yan J. G. et al., 2017b, Astrophys. Space Sci., 362, 236

SUPPORTING INFORMATION

Supplementary data are available at *MNRAS* online.

Please note: Oxford University Press is not responsible for the content or functionality of any supporting materials supplied by the authors. Any queries (other than missing material) should be directed to the corresponding author for the article.

This paper has been typeset from a TEX/LATEX file prepared by the author.